

# Lawrence Berkeley National Laboratory

## LBL Publications

### Title

Spatiotemporal mapping of microscopic strains and defects to reveal Li-dendrite-induced failure in all-solid-state batteries

### Permalink

<https://escholarship.org/uc/item/78x237fq>

### Authors

Shen, Hao  
Chen, Kai  
Kou, Jiawei  
[et al.](#)

### Publication Date

2022-07-01

### DOI

10.1016/j.mattod.2022.06.005

Peer reviewed

# **Spatiotemporal mapping of microscopic strains and defects to reveal Li-dendrite-induced failure in all-solid-state batteries**

Hao Shen<sup>1</sup>, Kai Chen<sup>1,\*</sup>, Jiawei Kou<sup>1</sup>, Zhanhui Jia<sup>1</sup>, Nobumichi Tamura<sup>2</sup>, Weibo Hua<sup>4</sup>,  
Wei Tang<sup>3,\*</sup>, Helmut Ehrenberg<sup>4</sup>, Marca Doeff<sup>5,\*</sup>

*1. Center for Advancing Materials Performance from the Nanoscale (CAMP-Nano),  
State Key Laboratory for Mechanical Behavior of Materials, Xi'an Jiaotong  
University, Xi'an, Shaanxi 710049, China*

*2. Advanced Light Source, Lawrence Berkeley National Laboratory, Berkeley, CA  
94720, USA*

*3. School of Chemical Engineering and Technology, Xi'an Jiaotong University, Xi'an,  
Shaanxi 710049, China*

*4. Institute for Applied Materials (IAM), Karlsruhe Institute of Technology (KIT),  
Hermann-von-Helmholtz-Platz 1, D-76344 Eggenstein-Leopoldshafen, Germany*

*5. Energy Storage and Distributed Resources Division, Lawrence Berkeley National  
Laboratory, Berkeley, CA 94720, USA*

## **Abstract**

Solid-state electrolytes (SSEs) are key to the success and reliability of all-solid-state lithium batteries, potentially enabling improvements in terms of safety and energy density over state-of-the-art lithium-ion batteries. However, there are several critical challenges to their implementation, including the interfacial instability stemming from the dynamic interaction of as-formed dendritic lithium during cycling. For this work, we emphasize the importance of studying the spatial distribution and temporal evolution of strains and defects in solid-state electrolytes at the micro-scale, and how this affects dendrite growth. A proof-of-principle study is demonstrated using the synchrotron radiation based micro Laue X-ray diffraction method, and a custom-developed in-situ cycling device. Defects and residual strains are observed near the Li-electrolyte interface and along the electrolyte grain boundaries, probably due to the sintering process during fabrication. As cycling proceeds, strain and defect concentrations are detected locally, which potentially evolve into weak points in the electrolytes. The feasibility of using this technique is discussed, and recommendations for micro strain engineering to address the Li/SSEs interfacial issues are given.

**Keywords:** all-solid-state Li battery; in-situ spatiotemporal  $\mu$ Laue study; microscopic strain and defects; dendritic failure.

## 1. Introduction

Ever growing demands for higher energy density and better safety in energy storage devices are prompting development of solid-state electrolytes (SSEs), construction of all-solid-state Li batteries (ASSLBs), and extended applications in not only electric vehicles and cell phones, but also airplanes and smart-grids.<sup>1,2</sup> SSEs potentially offer extraordinary advantages in reducing battery-stack volumes using a bipolar-stacked cell structure, which can potentially increase the energy densities of lithium batteries by 50% on both the device and system level.<sup>3</sup> The wide operating temperature range of SSEs can also reduce the requirement for heating/cooling modules with benefits for both energy efficiency and system cost.<sup>3,4</sup> Since the 1960s, the scientific community has witnessed the development of diverse varieties of SSEs, many of which have excellent temperature, moisture, and electrochemical stability, high ionic conductivity, good mechanical properties, and can be processed easily.<sup>5-8</sup>

Despite these advantages, ASSLBs still face several hurdles before they can be used in large-scale applications, such as maintaining intimate interfaces between lithium and the SSE. One of the critical challenges is the anodic failure stemming from undesirable Li dendrite or filament growth, once the cells are cycled above a critical current density.<sup>9,10</sup> Unfortunately, this is often too low to guarantee an acceptable performance.<sup>10,11</sup> The growth of Li dendrites also makes fast charge and long cycle life difficult to attain. Although it is theoretically predicted that Li dendrites can be suppressed once the shear module of the SSE exceeds twice of that of Li metal (4.8 GPa at room temperature),<sup>12</sup> Li dendrites are still observed in many SSEs with the

mechanical properties satisfying the criterion. For example, Li dendrites are detected in LLZO, the shear modulus of which is over 50 GPa, more than 10 times higher than Li.<sup>13-15</sup> Considerable effort has been made to optimize the microstructures of the SSEs by changing the interface, density, grain size, and so on,<sup>16-20</sup> with only limited success. There has been a long-lasting debate over the interaction mechanism between Li metal and SSEs as well as the exact origins for the formation of dendritic Li in SSEs.<sup>21-23</sup> Studies have been carried out to investigate this question using a variety of characterization techniques. As shown in Figure 1, battery cycling tests have revealed the influence of interfacial resistance.<sup>11,24</sup> Optical and scanning electron microscopes (SEM) have been used to directly visualize the growth of dendrites, starting from flaws and then growing either along or across the grains.<sup>10,11</sup> Transmission electron microscopy (TEM) and computed tomography (CT) provide a direct link of microstructure to dendrite formation,<sup>25,26</sup> while chemical mapping studies highlight the spatial and temporal distribution of elements<sup>26-31</sup>.

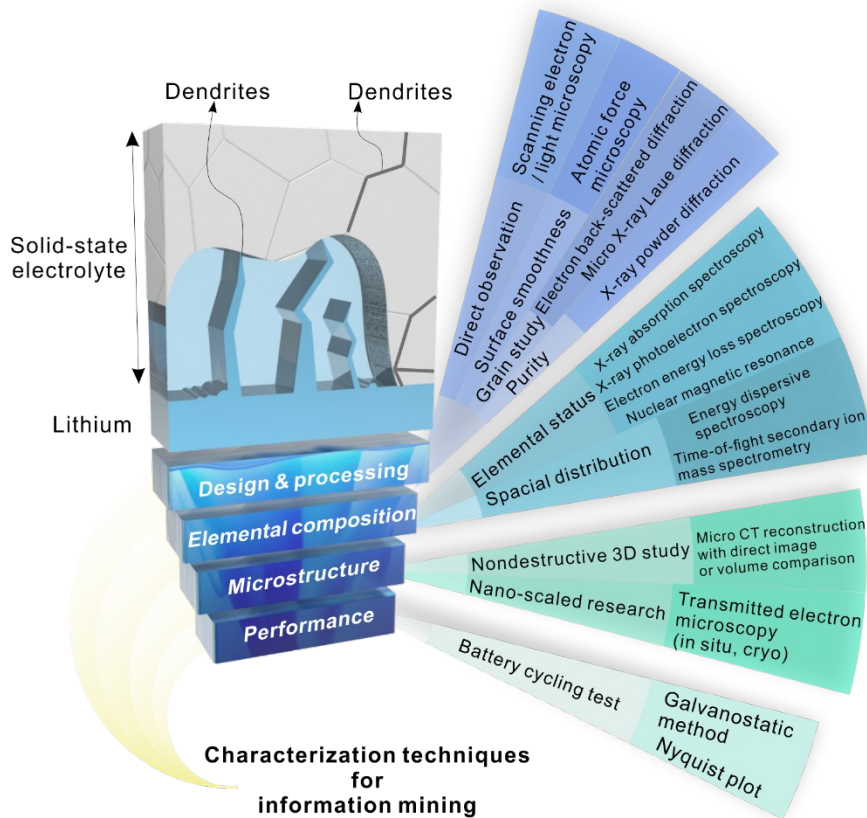


**Figure 1** Characterization techniques applied in the main procedures from design & processing to performance testing of ASSLBs that are related to Li-induced failure.

These efforts have shed light on the growth of Li dendrites associated with the electrochemical and mechanical synergy effects at the Li/SSEs interface, and two mechanisms have been proposed independently. These are electric field enhanced mechanical penetration and electronic conduction induced Li dendrite formation. The former proposes that the preferred nucleation sites arise from or near the Li/SSE interface and dendrites grow directionally penetrating the SSEs. The latter emphasizes the co-relationship between the formation of lithium dendrites and the intrinsic properties of SSEs such as relatively high electronic conductivity, causing more uniform Li deposition inside the SSEs. Both mechanisms are supported by some

theories and experiments but they cannot explain all phenomena observed. To date, the common mechanism for the complicated interaction between lithium anodes and SSEs remains unclear.

In the next section, we will compare the existing viewpoints on the interaction between Li and SSEs and the mechanisms in the SSE.<sup>20,23,32</sup> Although focusing on different aspects, researchers agree on the importance of novel and powerful materials characterization methods.<sup>23,33</sup> By comparing the viewpoints of these two mechanisms, we emphasize that microscopic strain, elastic and plastic, plays a key role in Li dendrite growth resulting in anodic failure as reported previously, and then highlight two key points for distinguishing the two major mechanisms of Li dendrite growth and optimization of the design of SSEs. First is mapping of the localized strains and stresses, and correlating them to the microscopic defects which originate during fabrication and processing stages, or generated during service. Second is monitoring the evolution of strains, stress, and defects under service conditions over a relatively long period of time, from the stage prior to Li dendrite nucleation until growth and short-circuit failure. Here, we apply synchrotron radiation based micro Laue X-ray diffraction ( $\mu$ Laue) to investigate strains and defects distribution in a millimeter-sized crystalline SSE, mapped with micro-scale resolution, using a custom-developed data mining method. Powered by an in-house designed in-situ cycling apparatus, the temporal evolution of strains and defects was studied to correlate the electrochemical and mechanical behaviors under operando conditions at the early stages, even before Li dendrite nucleation. This powerful materials characterization technique, can

provide a more comprehensive explanation to the incipience of dendritic Li in SSEs by electro-chemo-mechanical coupled effects, and provides insights into effective design and engineering of SSEs.

## **2. Mechanisms of Li dendrite formation in solid-state electrolyte**

### **2.1 Electric field enhanced mechanical penetration**

Electric field enhanced mechanical penetration emphasizes the importance of electric field concentrators such as imperfect contact at the interface of Li/SSE. Li infiltrates at pre-existing defects preferentially and eventually causes short-circuit failures. Operando optical microscopy experiments showed crack generation in polycrystalline, single-crystalline, and glassy SSEs from the contact point where the Li deposited (Figure 2a upper).<sup>10</sup> The continuous Li plating in the flaws resulted in stress build-up due to the constrained situation and opened up cracks. The stress generated is directly proportional to the overpotential, while the minimum stress needed for crack propagation is materials and geometry dependent. Thus, by considering the elastic properties of Li, an inverse square root relationship can be established to describe the Li plating overpotential and crack-propagation stress as a function of defect size.<sup>10</sup> Similar phenomena have also been observed using other techniques. Zhang et al. reported an operando study of Li whisker growth kinetics in an environmental TEM equipped with an atomic force microscope tip, which allowed application of a potential and recording of the stress generated simultaneously (Figure 2a bottom).<sup>34</sup> Under such electro-chemo-mechanical coupled circumstances, the yield

strength of micro-sized Li whiskers, which is crystal direction- and size-dependent, was up to two orders of magnitude greater of that of their polycrystalline bulky counterparts. Based on the elastic and plastic properties of Li whiskers, a new elastoplastic model was developed, explaining the existence of critical flaw size on the order of hundred  $\mu\text{m}$ , under which no Li whisker would grow no matter how high the overpotential was.<sup>10</sup> In an SEM study, void formation induced SSE/anode interface failure was revealed as the cells were cycled, due to the slow replenishment rate as the Li was stripped, indicating that the elimination of pre-existing defects on the surface of SSEs was not enough to prevent formation of Li whiskers.<sup>35,36</sup> On the other hand, pressure-induced Coble creep of Li was shown by operando TEM experiments to be an effective approach to fill in hollow ionically and electronically conducting tubules, which allows replenishment of the stripping-induced Li loss and thus releases the stresses at the interface.<sup>37</sup>

Thanks to the high penetration capability of high-energy X-rays and neutron beams, 3D imaging techniques such as computed tomography (CT) have been developed to visualize the structure of SSEs (even those that contain heavy elements) with decent spatial resolution.<sup>31,38-40</sup> Taking advantages of these features, interphase formation was evidenced directly in Li/Li<sub>10</sub>SnP<sub>2</sub>S<sub>12</sub>/Li cells.<sup>31</sup> Voids formed at the interface and caused large area of contact loss between Li and SSE (Figure 2b left). Through quantitative imaging correlation and comparison, the cell was proven to undergo a volume shrinkage due to the partial molar volume mismatch between electrodes, suggesting the importance of controlling stack stress in the all-solid-state

cells.<sup>31</sup>

Along with the electric field enhanced mechanical penetration mechanism, some specific crack modes have been reported. For example, so-called spallation cracking was observed in a Li/Li<sub>6</sub>PS<sub>5</sub>Cl/Li symmetrical cell (Figure 2b right), mostly in the area with high incidence of porosity, as well as the edges and corners of the electrodes where the electric field was higher due to geometrical crowding factors.<sup>30</sup> Combining CT and X-ray diffraction mapping, it was also shown that Li filling in the crack tips was not necessary for crack opening. Similarly, “bowl-like” cracks were discovered inside the SSE in Li/Li<sub>6.4</sub>La<sub>3</sub>Zr<sub>1.4</sub>Ta<sub>0.6</sub>O<sub>12</sub> (LLZTO) half-cells, stressing that attention should be paid to not only the interface but also the bulk of SSEs.<sup>41</sup>

In general, the electric field enhanced mechanical penetration mechanism emphasizes the failure caused by mechanical cracking and Li deposition in the cracks. It is featured by: (1) unbalanced Li stripping and plating that result in local high electric field; (2) directional crack propagation and Li infiltration starting from or near the interface; (3) continuous Li deposition as the driving force for cracks to extend; (4) significant strain/stress concentration. Based on this mechanism, to produce an SSE with improved stability under high current density, it is essential to accelerate the replenishment rate of Li, control the strain/stress at the interface, achieve high density SSEs with smooth surfaces, and optimize the mechanical properties of SSEs to resist crack growth.

## **2.2 Electronic conductivity facilitated mechanism**

In some cases, increasing the density of SSEs to modify the interfacial quality as

well as strengthening their mechanical properties does not eliminate Li dendrite formation completely. Considering that Li is frequently preferentially deposited along the grain boundaries, where the electronic conductivity may be higher than in the interior of crystal grains, an electronic conductivity facilitative mechanism is proposed. For this mechanism, the Li dendrite generation is electrochemically activated in an “overcome strength with softness” manner. The Li ions are reduced easily once meeting the free-traveling electrons and then Li dendrites nucleate at relatively arbitrary possible locations without depth preferences inside the SSEs. This mechanism also explains the proportional growth of critical current density with the operating temperature. At elevated temperatures, the Li/SSE interface quality is usually improved and thus accelerates the movement of ions and electrons to form a larger number of nucleation sites for Li dendrites. A short circuit does not occur because the surface area of Li dendrites decreases and minimizes the chances to interconnect.

The operando neutron depth profiling technique, which relies on the interaction between  ${}^6\text{Li}$  isotopes and neutrons, has been used to detect the Li concentration in SSEs.<sup>33</sup> The depth resolution of this method can be as good as tens of nanometers.<sup>42</sup> Interestingly, according to a comprehensive study of various SSEs including lithium phosphorus oxynitride, lithium lanthanum zirconium oxide (LLZO), and  $\text{Li}_3\text{PS}_4$ , the concentration profile of Li showed no depth-dependence (Figure 2c), which is significantly different from the mechanical penetration mechanism. Operando TEM observations (Figure 2d upper) and electron energy loss spectroscopy (EELS)

provided direct evidence of Li deposition along grain boundaries, where the band gap decreases and electrons move more actively. Consequently, Li reduced and nucleated at the grain boundaries, grew along them, connected and finally shorted the batteries.<sup>26</sup> Monte Carlo simulations with similar results suggest that low energy grain boundaries are crucial for high ion transference (Figure 2d bottom).<sup>43</sup> According to Li and Monroe's modeling work, the capacitive Li/SSE interface offered a space charge layer, which imposed compressive stresses onto the interface. The compressive stresses prompt the Li to deposit along grain boundaries instead of at interfaces, demonstrating that the size and shape of grains and misorientation between neighboring grains are important to Li dendrite growth<sup>44</sup>. This also explains why the critical current density is dependent of the microstructures of LLZO.<sup>29,45</sup>

According to the investigations, the electronic conductivity facilitated mechanism is characterized by: (1) depth/surface insensitivity and insignificant directional penetration; (2) grain boundaries as favorable nucleation sites in polycrystalline SSEs; (3) non-essential strain/stress concentration. Based on this mechanism, reducing the electronic conductivity of SSEs is the most critical way to improve performance.

These two mechanisms highlight the different characteristics of Li dendrite growth in SSEs and point to different optimization pathways. However, these two mechanisms are supported by different experimental observations and theoretical predictions independently. It is even possible that the two mechanisms co-exist and contribute together to the short-circuit failure. It should also be noted that the failure

mode highly depends on the chemistry, microstructure and working conditions of the batteries. These questions are still open for many reasons, one of which is the lack of characterization tools to monitor the driving force for Li dendrite to incubate and nucleate. At such an early stage, although it is apparent that strain/stress plays an important role, Li dendrites are too tiny to see, and thus researchers face difficulties in determining the area of interests for in-depth study. As a result, it is extremely important to develop a powerful strain/stress characterization tool with nano/micro-scale spatial resolution, millimeter-scale sampling size, decent temporal resolution, and easy to nondestructive operando observations simultaneously. With these advantages, it becomes possible to correlate the early-stages of Li deposition, in space and time, to the strain/stress distribution and evolution, and eventually improve the electro-chemo-mechanical performance of SSEs by means of microstructure design and processing optimization.

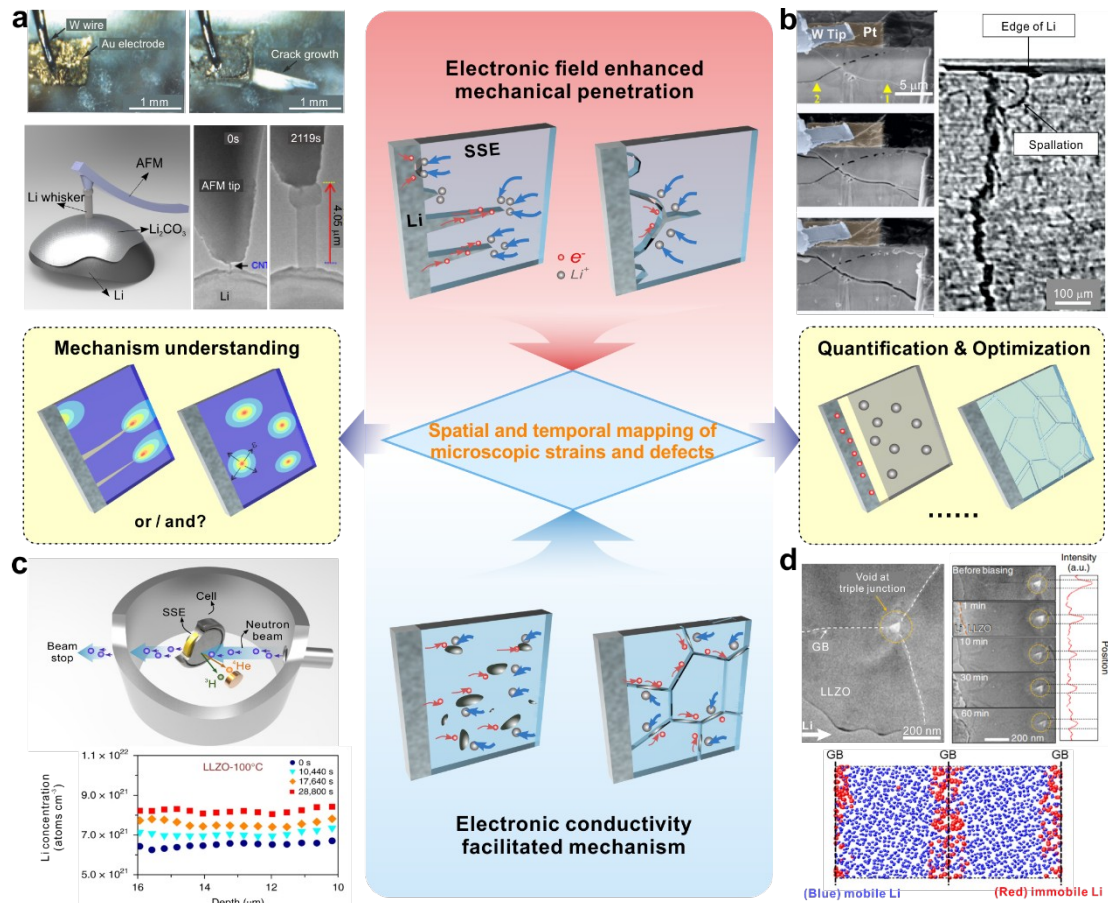


**Figure 2** Typical experiments that support the electric field enhanced mechanical penetration are shown in (a) and (b), and that support electronic conductivity are shown in (c) and (d). The upper of (a) presents the operando experiment under optical microscope (*reproduced from Ref. 10 with permission from Wiley-VCH*). The bottom of (a) is an operando experiment on the ETEM-AFM platform (*the Li whisker figure is reproduced from Ref. 35 with permission from Nature*). The bottom-left of (a) shows the setup of the platform. (b) shows the interfacial evolution (left, *reproduced from Ref. 32 with permission from Nature*) and spallation crack formation (right, *reproduced from Ref. 31 with permission from Nature*) visualized by CT. (c) is the setup and result of NDP experiment (*the NDP result is reproduced from Ref. 34 with permission from Nature*). The in situ TEM (upper, *reproduced from Ref. 26 with permission from Nature*) and Monte Carlo (bottom, *reproduced from Ref. 44 with permission from American Chemistry Society*) results shows the behavior of grain boundary in (b). Through comparing the two mechanisms, spatial and temporal mapping of microscopic strains and defects are key to understanding Li-dendrite-induced failure in ASSLBs.

### 3. Microstructure and microstrain mapping by $\mu$ Laue

#### 3.1 Principle

Synchrotron radiation based micro Laue X-ray diffraction ( $\mu$ Laue) is a promising tool for characterizing SSEs because of its high spatial (submicron), strain ( $10^{-4}$ ), and

temporal (sub-second for each spot) resolutions. In a typical  $\mu$ Laue setup, a polychromatic X-ray beam, focused to submicron size using a pair of elliptically shaped mirrors, illuminates the specimens with crystal grains larger than the X-ray beam size and generates Laue diffraction.<sup>46</sup> High accuracy multi-axis-motion sample stage allows the area of interest on the specimen to be scanned, and at each scanning position, with only a sub-second single exposure, a Laue pattern is recorded using a large-area 2D detector. In most cases, the experiments are carried out in reflection geometry; transmission mode is performed for thin foils only. A typical  $\mu$ Laue scan generates thousands of Laue diffraction patterns, each of which contains rich local microstructural information. Thus, by analyzing all the Laue patterns, the distribution of crystal structure, orientation, deviatoric elastic strain, and microscopic defects such as vacancies and dislocations in the scanned area can be mapped, and the spatial resolution is only limited by X-ray beam size and scanning step size. In addition, by inserting a monochromator in the path of the beam and tilting its incline angle in minute steps, the energy of the incident X-ray is finely scanned. This so-called energy scan is equivalent to the rocking curve measurement in conventional XRD, with which local lattice constants can be measured accurately. A Si-drift detector frequently equipped a  $\mu$ Laue beamline to enable micro X-ray fluorescence chemical analysis.

From the description above, it is clear that  $\mu$ Laue differs significantly from powder diffraction. Conventional powder diffraction employs monochromatic X-ray to irradiate a great number of crystal grains to produce signals. With proper data processing, crystal structure, grain size and preferred orientations can be analyzed, but

little can be known about the spatial distribution of crystal orientation, strain, and microscopic defects at the intragranular scale.<sup>47</sup> Such information is important to in-depth understand the performance of SSEs and accessible using  $\mu$ Laue.

To demonstrate its application, the microstructure of LLZO in a symmetric Li/LLZO/Li cell was characterized using  $\mu$ Laue. The LLZO used for this test was synthesized and processed following the typical sintering procedure, and the final sample thickness was 1.11 mm and the relative density was about 90%. As displayed in Figure 3a, the cell was mounted on the scanning stage with its cross-section facing up to the micro-focused polychromatic X-ray with an incline angle of 45°. A  $260 \times 260 \mu\text{m}^2$  area covering the Li/LLZO interface was raster scanned with a scanning step size of  $2 \mu\text{m}$  (Figure 3b). Because of the poor crystallinity and low diffraction intensity of Li, only LLZO diffraction patterns were analyzed. Clearly, the Laue patterns from different grains appear quite different, and also the diffraction peak width varied from grain boundary vicinities to the interiors. By analyzing all the 16900 Laue patterns using a custom-developed software XMAS<sup>48</sup> and the peak position comparison indexing algorithm<sup>49</sup>, crystal orientation, elastic deviatoric strain (all 6 components of the tensor as well as the von Mises equivalent strain), and diffraction peak width, which is an indicator of the microscopic defects, were successfully mapped (Figure 3c). Three crystal grains were detected in the scanned region. The strain was lower than  $0.5 \times 10^{-3}$  on average and was high near the Li/LLZO interface. Microscopic defects were distributed in the LLZO inhomogeneously, mostly lying near the interface and along the grain boundaries.

Although an energy scan was not carried out on this specimen, the diffraction peaks from two phases with a lattice mismatch of  $0.5 \times 10^{-3}$  could be unequivocally distinguished (Figure 3d). The lattice mismatch accuracy is also dependent on crystal size, quality, and chemical composition, etc.

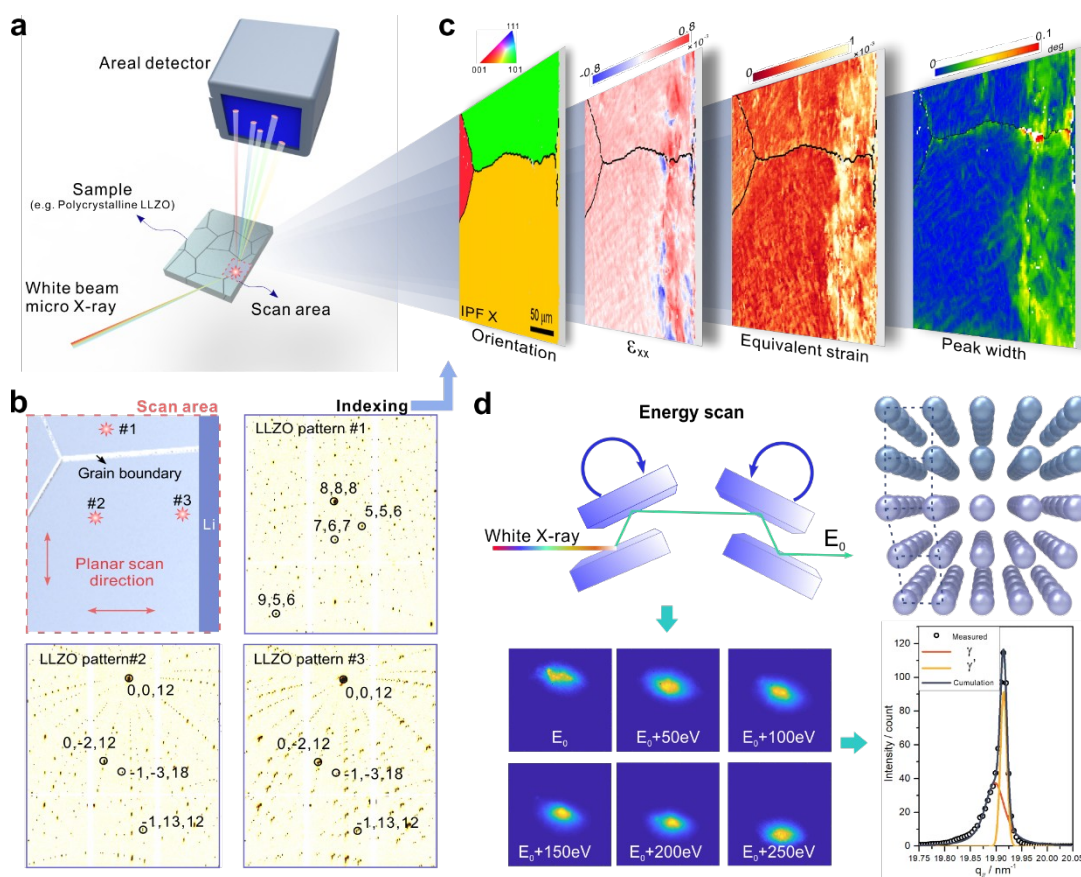


**Figure 3** The setup of  $\mu$ Laue is presented in (a). (b) gives the comparison of Laue diffraction patterns in two grains (#1 and #2) and large deformation in one grain (#2 and #3). After indexing the patterns, the mappings of orientation, components of strain tensors, Von Mises equivalent strain, and peak width can be achieved in (c). The description of energy scan is shown in (d) where the upper figure shows the setup and the bottom figure shows the diffraction peak evolution with the tilt of monochromators. The mismatch of two phases is obtained in the bottom-right figure of (d).

### 3.2 Operando $\mu$ Laue study

To enable the operando  $\mu$ Laue study for the microstructure of SSEs under cycling conditions, an in-situ cycling apparatus was designed to contain two nested wide-open

chambers. As shown in Figure 4a, the same Li/LLZO/Li symmetric cell demonstrated in Figure 3 was fixed in the inner chamber, slightly compressed mechanically with a specially designed clampers to ensure electric contact between Li and SSE, and subjected to a constant current density of  $3.34 \mu\text{A}/\text{cm}^2$ . It should be noted that the applied voltage and/or current can be programmed and accurately controlled for various purpose of study. Once the specimen was well aligned, the inner chamber was placed into a bigger one, which was then sealed with Kapton tape, filled with protective Ar gas, and then mounted onto the scanning stage. After the first 2 hours (3 cycles) of electric current stressing, the same interfacial area was scanned, as shown in Figure 3. Then electrical cycling tests and  $\mu\text{Laue}$  scans were repeated one more time after another 24 hours cycling (16 cycles). In the last scan, the current density was doubled and continued with 3 hours cycling (3 cycles), and the same area was scanned. The scans were named Scan 1 to 3 in chronological order; as a baseline, the scan prior to current stressing (displayed in Figure 3) was named Scan 0.

From the strain maps (Figure S1 in Supplementary Materials), no significant change was detected. From a more detailed statistical comparison, for example in Figure 4a, lattice strains were generated as the symmetric cell was stressed under electric current. After mapping the  $\varepsilon_{zz}$  component of strain tensor which exhibits the strain evolution in the Z direction, the strain evolution from compression to tension is obvious (in Figure 4b), and this variation occurs in all the detected grains. It should be noticed that since the electric current was passed as the  $\mu\text{Laue}$  scans were performed, the strains reported here were residual strains rather than transient ones. During the

process, the intragranular misorientation also increased, which is especially obvious at the bottom right corner of the scan (Figure 4c). Statistically, the frequency-misorientation curve of Scan 3 shifted to higher angles (Figure 4d).

From these results, it appears that inhomogeneous residual strains were produced at the subsurface during fabrication and processing, which are more notable in larger samples. Secondly, at the early stage of electrical tests, obvious strain and microstructure evolution has been detected. Such evolution, as observed in the misorientation map, can be highly localized and concentrated, and thus likely to become the starting point of catastrophic failures. To verify this postulate, more investigations with longer cycling period of time and, maybe, larger scanned area are needed. Energy scan will be also helpful to answer directly whether lattice volume changes will occur due to ion transference and space charging, especially near the interface and grain boundaries. Many other open questions require more systematic study, for example, how testing temperature and interface modification influence strain distribution, how grain size and grain boundary types impact failure mode, and so on. The study of microstructure and strains with spatial and temporal resolution helps establish the relationship between fabrication parameters and electro-mechano-chemistry of SSEs, which can ultimately lead to improved performance of all-solid-state batteries.

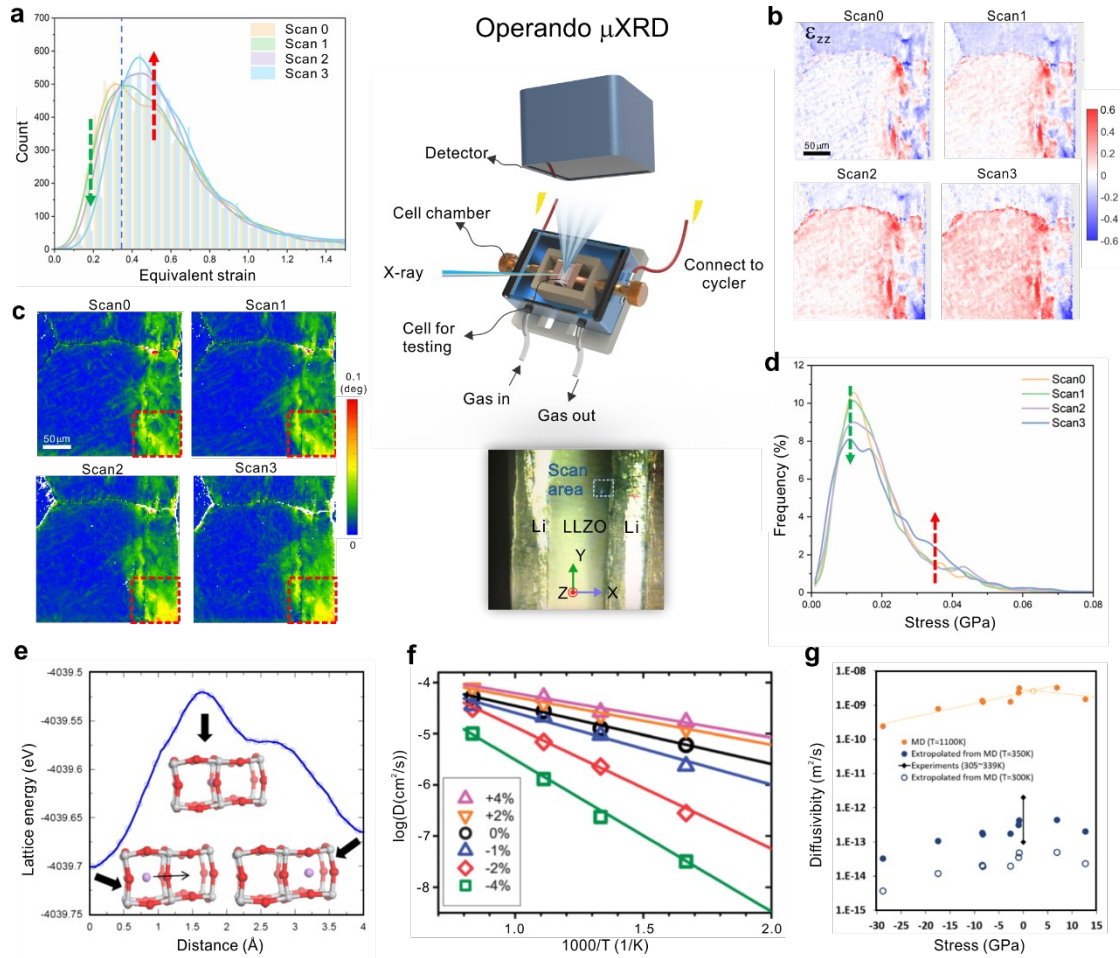


**Figure 4** The setup of operando  $\mu$ Laue is given in the middle of the figure. The insert is the optical photo of the detected Li/LLZO/Li cell. (a) shows the evolution of Von Mises equivalent strain of the near surface part, and (b) is the evolution of  $\epsilon_{zz}$  of the whole detected area. (c) is the intragranular misorientation mapping. Area in the red rectangle shows obvious increases in misorientation. The statistical study of intragranular misorientation of the same area as (a) is shown in (d). (e), (f). In (g) research results show how the lattice deformation can affect lithium lanthanum titanate (LLT) (*reproduced from Ref. 54 with permission from Royal Society of Chemistry*), lithium germanium phosphosulfide (LGPS) (*reproduced from Ref. 55 with permission from Elsevier*) and LLZO (*reproduced from Ref. 56 with permission from Elsevier*).

### 3.3 Qualification of strain and ionic conductivity in SSEs

Strains can be introduced into SSEs during the manufacturing, especially from the sintering procedure<sup>50,51</sup>, and can also accumulate during cycling either because of mass diffusion or volume changes stemming from the cathode<sup>52</sup>. Strain mapping is important not only for revealing the failure mechanism, but also for optimizing the

ionic conductivity via elastic strain engineering, because it has been proved that the distortion and dilatation of SSE lattices leads to variation in ionic migration barriers. Considering effects of the hydrostatic stress, or pressure, only, the ionic conductivity is expressed by the following equation:

$$\frac{\partial \ln(\sigma)}{\partial P} = \frac{\beta}{3} - \frac{V_a}{k_B T},$$

where  $\sigma$  is the ionic conductivity,  $P$  the pressure,  $\beta$  the material compressibility,  $V_a$  the activation volume,  $k_B$  the Boltzmann constant, and  $T$  the temperature.

The activation volume  $V_a$ , which could be either negative or positive,<sup>53</sup> is materials dependent. Compressive strain/stress promotes the ionic conductivity for materials with negative activation volume, such as Li- $\beta$ -Al<sub>2</sub>O<sub>3</sub>, but for K- $\beta$ -Al<sub>2</sub>O<sub>3</sub> the activation volume of which is positive, tensile stress/strain favors ionic conduction. Ion migration energy barriers increase when the applied strain results in a bottleneck for ion migration in lithium lanthanum titanate (LLT) with the perovskite structure (Figure 4e), and lithium germanium phosphosulfide (LGPS) (Figure 4f).<sup>54,55</sup> The mechanical pressure theoretically will impede ion transference in Na<sub>3</sub>PS<sub>4</sub> due to the lattice volume decrease, but better densification and mobile sodium defects can offset the negative influence.<sup>56</sup> Based on the recent simulations, the highest Li self-diffusivity is obtained in LLZO strained by 2 GPa tensile stress (Figure 4g).<sup>56</sup> Considering the existence of a large population of oxygen vacancies in LLZO, the induced strains are expected to influence Li ion transfer and phase stability.

Therefore, strain mapping benefits the processing of SSEs and the design of all

solid-state batteries, especially for the thick composite electrodes.

#### **4. Summary and Outlook**

In this article, we have introduced the two common proposed mechanisms for Li dendrite-induced short-circuit failure, and introduced the high-resolution microscopic strain and defect mapping technique as an important tool to better understand the incipience of Li dendrite formation in SSEs. The connection between strain and ionic conductivity is also emphasized. A proof of principle experiment has proven the feasibility of  $\mu$ Laue in operando SSE cycling studies.

Because the batteries are under an electro-chemo-mechanical multi-field coupled condition during service, it is necessary to develop a comprehensive characterization approach that visualizes the distribution and evolution of morphology, strain/stress, chemical concentration and valence state.<sup>57</sup> In line with this,  $\mu$ Laue can be combined with other synchrotron radiation based techniques such as micro/nano-CT, X-ray absorption spectroscopy, and X-ray absorption near edge structure spectroscopy<sup>58</sup> (Figure 5a) to collect the mechanical, chemical, electrical, and morphological information at multi-scale and dimensions simultaneously.

The recently developed technique, diffraction contrast tomography, realizes the function of both CT and  $\mu$ Laue to some extent<sup>59,60</sup> and has demonstrated the power to characterize the grain morphology, orientation, and strain/stress distribution in three dimensions. Diffraction contrast tomography has been successfully applied to study the grain boundary migration during grain growth in polycrystals (Figure 5b)<sup>61</sup>,

identify the 3D phase, grain and strain distribution in polycrystalline photovoltaic materials, and map the symmetry-breaking strain fields in ferroelectric ceramic materials<sup>62</sup>. This method is promising to shed light on understanding the interaction between Li metal and SSEs.

So far there are limited reports on the combination of spectroscopic and diffraction methods, and the difficulty lies in the fact that different types of detectors and sample environments are required for these techniques and the wavelength and collimation of the incident X-ray beams are different. It is equally important to cross check the synchrotron results with TEM, which provides unprecedented spatial resolution down to the sub-atomic scale. The combination of these techniques not only provides the comprehensive information of electrochemical and structural characteristics of the batteries, but also covers a larger portion of the specimens, avoiding the disadvantages of either poor spatial resolution or lack of representativeness suffered by the individual characterization techniques.

It is also essential to upgrade the in-situ cycling devices in at least two aspects. First, the design needs to be modified to meet the demands of multiple synchrotron techniques. In particular, a better window needs to be designed and fabricated for lower absorption, in order to minimize the influence on spectroscopic study. Second, as mentioned, external force and temperature exert significant influence on the performance of batteries. Thus, it is necessary to implement the temperature and displacement/force control modules into the in-situ cycling stage (Figure 5c).

More sophisticated battery designs may be required, e.g.; using 3D composite

electrode and/or electrolyte frames<sup>8,63-69</sup> to improve energy density, relieving stresses from Li metal by Coble creep<sup>37</sup>, and using multilayer composite solid electrolytes.<sup>70, 71</sup> When innovative 3D structures are applied in all-solid-state batteries (Figure 5d), more detailed studies need to be executed, for instance the strain distribution in multiple dimensions, lattice mismatch control at the interface, and geometric structure control.

With various characterization techniques applied to all-solid-state battery study, microscopic strain and defects can be mapped with high spatial and temporal resolutions, and their evolution may be directly correlated to the electro-chemo-mechanical conditions and processes. These multi-dimensional and scale poly-therapeutic studies will provide important information, which can pave the way to all-solid-state batteries with high stability and long cycling life.

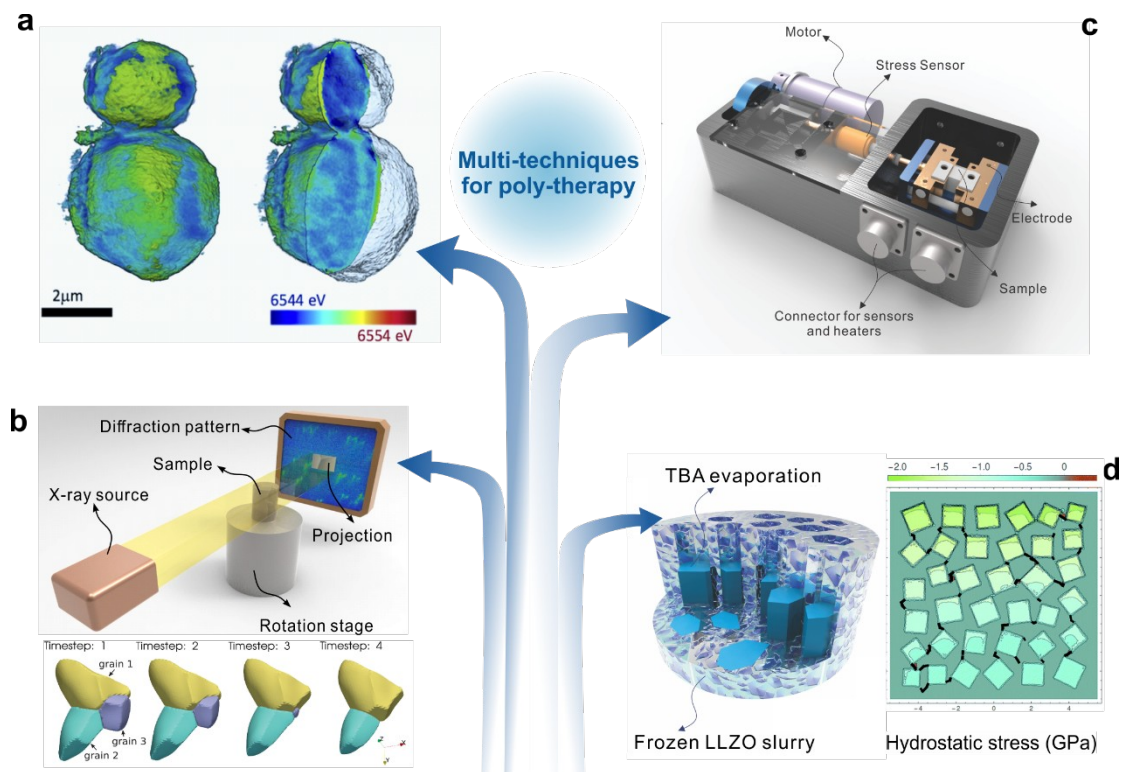


**Figure 5** Combination of multi characterization techniques can benefit further study, including (a) the combination of elemental mapping and tomography (*reproduced from Ref. 58 with permission from Elsevier*), (b) multi-field  $\mu$ Laue experiment, and (c) DCT (*the bottom figure is reproduced from Ref. 61 with permission from Elsevier*). For the composite electrode with SSE framework as (d), the strain mapping is also essential (*left figure is reproduced from Ref. 68 with permission from Royal Society of Chemistry, right figure is reproduced from Ref. 52 with permission from Royal Society of Chemistry*).

## References:

1. Xia, S., Wu, X., Zhang, Z., Cui, Y., Liu, W. (2019). Practical challenges and future perspectives of all-solid-state lithium-metal batteries. *Chem* 5, 753-785.
2. Gao, X., Zhou, Y.N., Han, D., Zhou, J., Zhou, D., Tang, W., Goodenough, J.B. (2020). Thermodynamic understanding of li-dendrite formation. *Joule* 4, 1864-1879.
3. Famprikis, T., Canepa, P., Dawson, J.A., Islam, M.S., Masquelier, C. (2019). Fundamentals of inorganic solid-state electrolytes for batteries. *Nat. Mater.* 18, 1278-1291.
4. Bai, P., Li, J., Brushett, F.R., Bazant, M.Z. (2016). Transition of lithium growth mechanisms in liquid electrolytes. *Energy Environ. Sci.* 9, 3221-3229.
5. Zhang, Z., Shao, Y., Lotsch, B.V., Hu, Y.-S., Li, H., Janek, J., Nan, C., Nazar, L., Maier, J., Armand, M. (2018). New horizons for inorganic solid state ion conductors. *Energy Environ. Sci.* 11, 1945-1971.
6. Afyon, S., Krumeich, F., Rupp, J.L.M. (2015). A shortcut to garnet-type fast Li-ion conductors for all-solid state batteries. *J. Mater. Chem. A* 3, 18636-18648.
7. Han, F., Zhu, Y., He, X., Mo, Y., Wang, C. (2016). Electrochemical Stability of  $\text{Li}_{10}\text{GeP}_2\text{S}_{12}$  and  $\text{Li}_7\text{La}_3\text{Zr}_2\text{O}_{12}$  Solid Electrolytes. *Adv. Energy Mater.* 6, 1501590.
8. Shen, H., Yi, E., Cheng, L., Amores, M., Chen, G., Sofie, S.W., Doeff, M.M. (2019). Solid-state electrolyte considerations for electric vehicle batteries. *Sustain. Energy Fuels* 3, 1647-1659.
9. Cheng, E.J., Sharafi, A., Sakamoto, J. (2017). Intergranular Li metal propagation through polycrystalline  $\text{Li}_{6.25}\text{Al}_{0.25}\text{La}_3\text{Zr}_2\text{O}_{12}$  ceramic electrolyte. *Electrochim. Acta* 223, 85-91.
10. Porz, L., Swamy, T., Sheldon, B.W., Rettenwander, D., Frömling, T., Thaman, H. L., Berendts, S., Uecker, R., Carter, W. C., Chiang, Y.-M. (2017) Mechanism of Lithium Metal Penetration through Inorganic Solid Electrolytes. *Adv. Energy Mater.* 7, 1701003.
11. Sharafi, A., Meyer, H. M., Nanda, J., Wolfenstine, J., Sakamoto, J. (2016). Characterizing the  $\text{Li-Li}_7\text{La}_3\text{Zr}_2\text{O}_{12}$  interface stability and kinetics as a function of temperature and current density. *J. Power Sources* 302, 135-139.
12. Monroe, C., Newman, J. (2005) The impact of elastic deformation on deposition kinetics at lithium/polymer interfaces. *J. Electrochem. Soc.* 152, A396-A404.
13. Ni, J.E., Case, E.D., Sakamoto, J.S., Rangasamy, E., Wolfenstine, J.B. (2012).

- Room temperature elastic moduli and Vickers hardness of hot-pressed LLZO cubic garnet. *J. Mater. Sci.* *47*, 7978-7985.
14. Ren, Y., Shen, Y., Lin, Y., Nan, C.-W. (2015) Direct observation of lithium dendrites inside garnet-type lithium-ion solid electrolyte. *Electrochem. Commun.* *57*, 27-30.
  15. Wang, A.-N., Nonemacher, J.F., Yan, G., Finsterbusch, M., Malzbender, J., Krüger, M. (2018) Mechanical properties of the solid electrolyte Al-substituted Li<sub>7</sub>La<sub>3</sub>Zr<sub>2</sub>O<sub>12</sub> (LLZO) by utilizing micro-pillar indentation splitting test. *J. Eur. Ceram. Soc.* *38*, 3201-3209.
  16. Han, X., Gong, Y., Fu, K.K., He, X., Hitz, G.T., Dai, J., Pearse, A., Liu, B., Wang, H., Rubloff, G., et al. (2017). Negating interfacial impedance in garnet-based solid-state Li metal batteries. *Nat. Mater.* *16*, 572-579.
  17. Cheng, L., Crumlin, E.J., Chen, W., Qiao, R., Hou, H., Lux, S.F., Zorba, V., Russo, R., Kostecki, R., Liu, Z., et al. (2014). The origin of high electrolyte–electrode interfacial resistances in lithium cells containing garnet type solid electrolytes. *Phys. Chem. Chem. Phys.* *16*, 18294-18300.
  18. Duan, H., Yin, Y.X., Shi, Y., Wang, P.F., Zhang, X.D., Yang, C.P., Shi, J.L., Wen, R., Guo, Y.G., Wan, L.J. (2018). Dendrite-free Li-metal battery enabled by a thin asymmetric solid electrolyte with engineered layers. *J. Am. Chem. Soc.* *140*, 82-85.
  19. Wang, C., Xie, H., Zhang, L., Gong, Y., Pastel, G., Dai, J., Liu, B., Wachsman, E.D., Hu, L. (2017). Universal soldering of lithium and sodium alloys on various substrates for batteries. *Adv. Energy Mater.* *8*, 1701963.
  20. Wang, C., Fu, K., Kammampata, S.P., McOwen, D.W., Samson, A.J., Zhang, L., Hitz, G.T., Nolan, A.M., Wachsman, E.D., Mo, Y., et al. (2020). Garnet-type solid-state electrolytes: materials, interfaces, and batteries. *Chem. Rev.* *120*, 4257-4300.
  21. Liu, J., Yuan, H., Liu, H., Zhao, C.-Z., Lu, Y., Cheng, X.-B., Huang, J.-Q., Zhang, Q. (2021). Unlocking the failure mechanism of solid state lithium metal batteries. *Adv. Energy Mater.* 2100748.
  22. Song, Y., Yang, L., Zhao, W., Wang, Z., Zhao, Y., Wang, Z., Zhao, Q., Liu, H., Pan, F. (2019). Revealing the short-circuiting mechanism of garnet-based solid-state electrolyte. *Adv. Energy Mater.* *9*, 1900671.
  23. Tang, Y., Zhang, L., Chen, J., Sun, H., Yang, T., Liu, Q., Huang, Q., Zhu, T., Huang, J. (2021). Electro-chemo-mechanics of lithium in solid state lithium metal batteries. *Energy Environ. Sci.* *14*, 602-642.
  24. Glenneberg, J., Bardenhagen, I., Langer, F., Busse, M., Kun, R. (2017). Time resolved impedance spectroscopy analysis of lithium phosphorous oxynitride - LiPON layers under mechanical stress. *J. Power Sources* *359*, 157-165.
  25. Ma, C., Cheng, Y., Yin, K., Luo, J., Sharafi, A., Sakamoto, J., Li, J., More, K.L., Dudney, N.J., Chi, M. (2016). Interfacial Stability of Li Metal-Solid Electrolyte Elucidated via in Situ Electron Microscopy. *Nano Lett.* *16*, 7030-7036.
  26. Liu, X., Garcia-Mendez, R., Lupini, A.R., Cheng, Y., Hood, Z.D., Han, F., Sharafi, A., Idrobo, J.C., Dudney, N.J., Wang, C., et al. (2021). Local electronic

- structure variation resulting in Li ‘filament’ formation within solid electrolytes. *Nat. Mater.* *20*, 1485-1490.
27. Park, K., Yu, B.-C., Jung, J.-W., Li, Y., Zhou, W., Gao, H., Son, S., Goodenough, J.B. (2016). Electrochemical nature of the cathode interface for a solid-state lithium-ion battery: interface between LiCoO<sub>2</sub> and garnet-Li<sub>7</sub>La<sub>3</sub>Zr<sub>2</sub>O<sub>12</sub>. *Chem. Mater.* *28*, 8051-8059.
  28. Kubicek, M., Wachter-Welzl, A., Rettenwander, D., Wagner, R., Berendts, S., Uecker, R., Amthauer, G., Hutter, H., Fleig, J. (2017). Oxygen vacancies in fast lithium-ion conducting garnets. *Chem. Mater.* *29*, 7189-7196.
  29. Cheng, L., Park, J.S., Hou, H., Zorba, V., Chen, G., Richardson, T., Cabana, J., Russo, R., Doeff, M. (2014). Effect of microstructure and surface impurity segregation on the electrical and electrochemical properties of dense Al-substituted Li<sub>7</sub>La<sub>3</sub>Zr<sub>2</sub>O<sub>12</sub>. *J. Mater. Chem. A* *2*, 172-181.
  30. Ning, Z., Jolly, D.S., Li, G., De Meyere, R., Pu, S.D., Chen, Y., Kasemchainan, J., Ihli, J., Gong, C., Liu, B., et al. (2021). Visualizing plating-induced cracking in lithium-anode solid-electrolyte cells. *Nat. Mater.* *20*, 1121-1129.
  31. Lewis, J.A., Cortes, F.J.Q., Liu, Y., Miers, J.C., Verma, A., Vishnugopi, B.S., Tippens, J., Prakash, D., Marchese, T.S., Han, S.Y., et al. (2021) Linking void and interphase evolution to electrochemistry in solid-state batteries using operando X-ray tomography. *Nat. Mater.* *20*, 503-510.
  32. Hatzell, K.B., Chen, X.C., Cobb, C.L., Dasgupta, N.P., Dixit, M.B., Marbella, L.E., McDowell, M.T., Mukherjee, P.P., Verma, A., Viswanathan, V., et al. (2020) Challenges in lithium metal anodes for solid-state batteries. *ACS Energy Lett.* *5*, 922-934.
  33. Han, F., Westover, A. S., Yue, J., Fan, X., Wang, F., Chi, M., Leonard, D.N., Dudney, N.J., Wang, H., Wang, C. (2019). High electronic conductivity as the origin of lithium dendrite formation within solid electrolytes. *Nat. Energy* *4*, 187-196.
  34. Zhang, L., Yang, T., Du, C., Liu, Q., Tang, Y., Zhao, J., Wang, B., Chen, T., Sun, Y., Jia, P., et al. (2020). Lithium whisker growth and stress generation in an in situ atomic force microscope–environmental transmission electron microscope set-up. *Nat. Nanotechnol.* *15*, 94-98.
  35. Kasemchainan, J., Zekoll, S., Spencer Jolly, D., Ning, Z., Hartley, G.O., Marrow, J., Bruce, P.G. (2019). Critical stripping current leads to dendrite formation on plating in lithium anode solid electrolyte cells. *Nat. Mater.* *18*, 1105-1111.
  36. Krauskopf, T., Hartmann, H., Zeier, W. G., Janek, J. (2019) Toward a fundamental understanding of the lithium metal anode in solid-state batteries-an electrochemo-mechanical study on the garnet-type solid electrolyte Li<sub>6.25</sub>Al<sub>0.25</sub>La<sub>3</sub>Zr<sub>2</sub>O<sub>12</sub>. *ACS Appl. Mater. Interfaces* *11*, 14463-14477.
  37. Chen, Y., Wang, Z., Li, X., Yao, X., Wang, C., Li, Y., Xue, W., Yu, D., Kim, S.Y., Yang, F., et al. (2020). Li metal deposition and stripping in a solid-state battery via Coble creep. *Nature* *578*, 251-255.
  38. Kahl, W.-A., Hansen, C., Bach, W. (2016). A new X-ray-transparent flow-through reaction cell for a  $\mu$ -CT-based concomitant surveillance of the reaction progress of

- hydrothermal mineral–fluid interactions. *Solid Earth* 7, 651-658.
39. Song, B., Veith, G.M., Park, J., Yoon, M., Whitfield, P.S., Kirkham, M.J., Liu, J., Huq, A. (2018) Metastable  $\text{Li}_{1+\delta}\text{Mn}_2\text{O}_4$  ( $0 \leq \delta \leq 1$ ) Spinel Phases Revealed by in Operando Neutron Diffraction and First-Principles Calculations. *Chem. Mater.* 31, 124-134.
  40. Song, B., Dhiman, I., Carothers, J.C., Veith, G.M., Liu, J., Bilheux, H.Z., Huq, A. (2019). Dynamic Lithium Distribution upon Dendrite Growth and Shorting Revealed by Operando Neutron Imaging. *ACS Energy Lett.* 4, 2402-2408.
  41. Zhao, J., Tang, Y., Dai, Q., Du, C., Zhang, Y., Xue, D., Chen, T., Chen, J., Wang, B., Yao, J., et al. (2021). In situ observation of Li deposition-induced cracking in garnet solid electrolytes. *Energy Environ. Mater.* DOI: 10.1002/eem2.12261.
  42. Downing, R.G., Lamaze, G.P., Langland, J.K., Hwang, S.T. (1993). Neutron depth profiling: overview and description of NIST Facilities. *J. Res. Natl. Inst. Stand. Technol.* 98, 109-126.
  43. Yu, S., Siegel, D.J. (2017). Grain boundary contributions to Li-ion transport in the solid electrolyte  $\text{Li}_7\text{La}_3\text{Zr}_2\text{O}_{12}$  (LLZO). *Chem. Mater.* 29, 9639-9647.
  44. Li, G., Monroe, C.W. (2019). Dendrite nucleation in lithium-conductive ceramics. *Phys. Chem. Chem. Phys.* 21, 20354-20359.
  45. Sharafi, A., Haslam, C.G., Kerns, R.D., Wolfenstine, J., Sakamoto, J. (2017). Controlling and correlating the effect of grain size with the mechanical and electrochemical properties of  $\text{Li}_7\text{La}_3\text{Zr}_2\text{O}_{12}$  solid-state electrolyte. *J. Mater. Chem. A* 5, 21491-21504.
  46. Kunz, M., Tamura, N., Chen, K., MacDowell, A.A., Celestre, R.S., Church, M.M., Fakra, S., Domning, E.E., Glossinger, J.M., Kirschman, J. L., et al. (2009). A dedicated superbend x-ray microdiffraction beamline for materials, geo-, and environmental sciences at the advanced light source. *Rev. Sci. Instrum.* 80, 035108.
  47. Barai, P., Fister, T., Liang, Y., Libera, J., Wolfman, M., Wang, X., Garcia, J., Iddir, H., Srinivasan, V. (2021). Investigating the calcination and sintering of  $\text{Li}_7\text{La}_3\text{Zr}_2\text{O}_{12}$  (LLZO) solid electrolytes using operando synchrotron x-ray characterization and mesoscale modeling. *Chem. Mater.* 33, 4337-4352.
  48. Tamura, N. (2014). Strain and Dislocation Gradients from Diffraction: Spatially Resolved Local Structure and Defects. Barabash, R., and Ice, G., eds. (World Scientific), pp. 125–155.
  49. Kou, J., Chen, K., Tamura, N. (2018). A peak position comparison method for high-speed quantitative Laue microdiffraction data processing. *Scr. Mater.* 143, 49-53.
  50. Yamada, H., Ito, T., Hongahally Basappa, R., Bekarevich, R., Mitsuishi, K. (2017) Influence of strain on local structure and lithium ionic conduction in garnet-type solid electrolyte. *J. Power Sources* 368, 97-106.
  51. Vedula, V.R., Glass, S.J., Saylor, D.M., Rohrer, G.S., Carter, W.C., Langer, S.A., Fuller, E.R. (2001). Residual-stress predictions in polycrystalline alumina. *J. Am. Ceram. Soc.* 84, 2947-2954.
  52. Bucci, G., Swamy, T., Chiang, Y.-M., Carter, W. C. (2017). Modeling of internal

- mechanical failure of all-solid-state batteries during electrochemical cycling, and implications for battery design. *J. Mater. Chem. A* *5*, 19422-19430.
53. Famprakis, T., Kudu, O.U., Dawson, J.A., Canepa, P., Fauth, F., Suard, E., Zbiri, M., Dambournet, D., Borkiewicz, O. J., Bouyanfif, H., et al. (2020). Under pressure: mechanochemical effects on structure and ion conduction in the sodium-ion solid electrolyte Na<sub>3</sub>PS<sub>4</sub>. *J. Am. Chem. Soc.* *142*, 18422-18436.
  54. Ong, S.P., Mo, Y., Richards, W.D., Miara, L., Lee, H.S., Ceder, G. (2012). Phase stability, electrochemical stability and ionic conductivity of the Li<sub>10±1</sub>M<sub>2</sub>X<sub>12</sub> (M = Ge, Si, Sn, Al or P, and X = O, S or Se) family of superionic conductors. *Energy Environ. Sci.* *6*, 148-156.
  55. Chen, B., Ju, J., Ma, J., Du, H., Xiao, R., Cui, G., Chen, L. (2018). Strain tunable ionic transport properties and electrochemical window of Li<sub>10</sub>GeP<sub>2</sub>S<sub>12</sub> superionic conductor. *Comput. Mater. Sci.* *153*, 170-175.
  56. Qi, Y., Ban, C., Harris, S.J. (2020). A new general paradigm for understanding and preventing Li metal penetration through solid electrolytes. *Joule* *4*, 2599-2608.
  57. Ren, C., Jiang, L., Kou, J., Yan, S., Li, L., Liu, M., Dong, X., Chen, K., Li, Z., Li, Z., et al. (2021). Development of micro-Laue technique at Shanghai Synchrotron Radiation Facility for materials sciences. *Sci. China Mater.* *64*, 2348-2358.
  58. Kan, W.H., Deng, B., Xu, Y., Shukla, A.K., Bo, T., Zhang, S., Liu, J., Pianetta, P., Wang, B.-T., Liu, Y., et al. (2018). Understanding the effect of local short-range ordering on lithium diffusion in Li<sub>1.3</sub>Nb<sub>0.3</sub>Mn<sub>0.4</sub>O<sub>2</sub> single-crystal cathode. *Chem* *4*, 2108-2123.
  59. Reischig, P., King, A., Nervo, L., Viganó, N., Guilhem, Y., Palenstijn, W.J., Batenburg, K.J., Preuss, M., Ludwig, W. (2013). Advances in X-ray diffraction contrast tomography: flexibility in the setup geometry and application to multiphase materials. *J. Appl. Crystallogr.* *46*, 297-311.
  60. Bleuet, P., Welcomme, E., Dooryhee, E., Susini, J., Hodeau, J.L., Walter, P. (2008). Probing the structure of heterogeneous diluted materials by diffraction tomography. *Nat. Mater.* *7*, 468-472.
  61. Zhang, J., Ludwig, W., Zhang, Y., Sørensen, H.H.B., Rowenhorst, D.J., Yamanaka, A., Voorhees, P.W., Poulsen, H.F. (2020). Grain boundary mobilities in polycrystals. *Acta Mater.* *191*, 211-220.
  62. Simons, H., Haugen, A.B., Jakobsen, A.C., Schmidt, S., Stohr, F., Majkut, M., Detlefs, C., Daniels, J.E., Damjanovic, D., Poulsen, H.F. (2018). Long-range symmetry breaking in embedded ferroelectrics. *Nat. Mater.* *17*, 814-819.
  63. Baggetto, L., Niessen, R.A.H., Roozeboom, F., Notten, P.H.L. (2008). High energy density all-solid-state batteries: a challenging concept towards 3D integration. *Adv. Funct. Mater.* *18*, 1057-1066.
  64. Kim, K.J., Rupp, J.L.M. (2020). All ceramic cathode composite design and manufacturing towards low interfacial resistance for garnet-based solid-state lithium batteries. *Energy Environ. Sci.* *13*, 4930-4945.
  65. Fu, K., Gong, Y., Hitz, G.T., McOwen, D.W., Li, Y., Xu, S., Wen, Y., Zhang, L., Wang, C., Pastel, G., et al. (2017). Three-dimensional bilayer garnet solid

- electrolyte based high energy density lithium metal–sulfur batteries. *Energy Environ. Sci.* *10*, 1568-1575.
66. McOwen, D.W., Xu, S., Gong, Y., Wen, Y., Godbey, G.L., Gritton, J.E., Hamann, T.R., Dai, J., Hitz, G.T., Hu, L., et al. (2018). 3D-printing electrolytes for solid-state batteries. *Adv. Mater.* *30*, e1707132.
  67. Shen, H., Yi, E., Amores, M., Cheng, L., Tamura, N., Parkinson, D.Y., Chen, G., Chen, K., Doeff, M. (2019). Oriented porous LLZO 3D structures obtained by freeze casting for battery applications. *J. Mater. Chem. A* *7*, 20861-20870.
  68. Shen, H., Yi, E., Heywood, S., Parkinson, D.Y., Chen, G., Tamura, N., Sofie, S., Chen, K., Doeff, M.M. (2020). Scalable freeze-tape-casting fabrication and pore structure analysis of 3D LLZO solid-state electrolytes. *ACS Appl. Mater. Interfaces* *12*, 3494-3501.
  69. Yi, E., Shen, H., Heywood, S., Alvarado, J., Parkinson, D.Y., Chen, G., Sofie, S.W., Doeff, M.M., All-solid-state batteries using rationally designed garnet electrolyte frameworks. *ACS Appl. Energy Mater.* *3*, 170-175.
  70. Zhu, J., Li, X., Wu, C., Gao, J., Xu, H., Li, Y., Guo, X., Li, H., Zhou, W. (2021) A multilayer ceramic electrolyte for all-solid-state Li batteries. *Angew. Chem. Int. Ed. Engl.* *60*, 3781-3790.
  71. Pfenninger, R., Struzik, M., Garbayo, I., Stilp, E., Rupp, J.L.M. (2019). A low ride on processing temperature for fast lithium conduction in garnet solid-state battery films. *Nat. Energy* *4*, 475-483.